Silicon-nitride nanosensors toward room temperature quantum optomechanics

Serra, Enrico; Borrielli, Antonio; Marin, Francesco; Marino, Francesco; Malossi, Nicola; Morana, Bruno; Piergentili, Paolo; Prodi, Giovanni Andrea; Sarro, Pasqualina Maria; More Authors

DOI
10.1063/5.0055954

Publication date
2021

Document Version
Final published version

Published in
Journal of Applied Physics

Citation (APA)
Serra, E., Borrielli, A., Marin, F., Marino, F., Malossi, N., Morana, B., Piergentili, P., Prodi, G. A., Sarro, P. M., & More Authors (2021). Silicon-nitride nanosensors toward room temperature quantum optomechanics. *Journal of Applied Physics*, *130*(6), Article 064503. https://doi.org/10.1063/5.0055954

Journal of Applied Physics ARTICLE scitation.org/journal/jap

Silicon-nitride nanosensors toward room temperature quantum optomechanics

Cite as: J. Appl. Phys. **130**, 064503 (2021); doi: 10.1063/5.0055954
Submitted: 5 May 2021 · Accepted: 26 July 2021 ·
Published Online: 11 August 2021

Enrico Serra,[1,2,3,a)] Antonio Borrielli,[1,2] Francesco Marin,[4,5,6,7] Francesco Marino,[6,7] Nicola Malossi,[8,9] Bruno Morana,[3] Paolo Piergentili,[8,9] Giovanni Andrea Prodi,[10] Pasqualina Maria Sarro,[3] Paolo Vezio,[6,7] David Vitali,[8,9] and Michele Bonaldi[1,2]

AFFILIATIONS

[1]Institute of Materials for Electronics and Magnetism, IMEM-CNR, Trento unit c/o Fondazione Bruno Kessler, Via alla Cascata 56/C, IT-38123 Povo, Trento, Italy
[2]Istituto Nazionale di Fisica Nucleare (INFN), Trento Institute for Fundamental Physics and Application, Via Sommarive 14, IT-38123 Povo, Trento, Italy
[3]Department of Microelectronics, Delft University of Technology, Feldmannweg 17, 2628 CT Delft, The Netherlands
[4]Dipartimento di Fisica e Astronomia, Università di Firenze, Via Sansone 1, I-50019 Sesto Fiorentino (FI), Italy
[5]European Laboratory for Non-Linear Spectroscopy (LENS), Via Carrara 1, I-50019 Sesto Fiorentino (FI), Italy
[6]CNR-INO, L.go Enrico Fermi 6, I-50125 Firenze, Italy
[7]INFN, Sezione di Firenze, Via Sansone 1, I-50019 Sesto Fiorentino (FI), Italy
[8]Physics Division, School of Science and Technology, University of Camerino, Via Madonna delle Carceri 9, I-62032 Camerino (MC), Italy
[9]INFN, Sezione di Perugia, via A. Pascoli, I-06123 Perugia, Italy
[10]Dipartimento di Matematica, Università di Trento, I-38123 Povo, Trento, Italy

a)Author to whom correspondence should be addressed: E.Serra@tudelft.nl and enrico.serra@tifpa.infn.it

ABSTRACT

Micro- and nanomechanical resonators play a prominent part in many sensing and signal processing platforms due to their capability to pervasively couple with a wide variety of physical systems. Particularly relevant is their embedding in advanced optomechanical setups, which has recently pioneered optically cooled mechanical oscillators toward the quantum regime. A frequently adopted experimental scheme exploits a thin, highly tensioned Si_3N_4 nanomembrane where the membrane's vibrations are dispersively coupled to the optical mode of a Fabry–Pérot cavity. A significant effort has been done into realizing high-quality factor membranes, considering that low mechanical loss represents a benchmark to operate in the elusive quantum regime. In this article, we compare two state-of-the-art SiN resonators, realized exploiting the dilution of the material's intrinsic dissipation and efficient solutions to fully isolate the membrane from the substrate. In particular, we examine and discuss the interplay between the edge and distributed dissipation and propose an analytical approach to evaluate the total intrinsic loss. Also, our analysis delves into the sensitivity of the devices to a point-like force and a uniform-density force field. These results provide meaningful guidelines for designing new ultra-coherent resonating devices.

I. INTRODUCTION

Micro- and nano-mechanical systems are broadly employed in many technological areas to sense, transduce, and process electromagnetic signals. A striking example is cavity optomechanics, wherein light confinement allows for the coherent interaction of mechanical and optical modes, enabling both the mechanical control of optical fields and the optical manipulation of the state of mechanical elements. This field of research has seen impressive progress in recent years, also facilitated by the remarkable progress of nanofabrication techniques. Also, a significant effort has been

made to push optomechanical systems toward quantum operation, given the prominent and well-recognized role of quantum-limited sensing and metrology tools for growth and development in various fields such as healthcare, security, electronics industry, and research. This requires the realization of ultracoherent mechanical resonators combined with sophisticated protocols of measurement and control of both mechanical motion and the optical field. Soft-clamped SiN nanomembranes embedded in a Fabry–Pérot cavity have demonstrated the feedback-based quantum control of mechanical motion[1] and sub-Standard Quantum Limit (SQL) displacement sensitivity,[2] while highly reflective silicon resonator has enabled the quantum non-demolition measurement of optical field fluctuations.[3] The domain of application of quantum-enhanced devices ranges from fundamental physics experiments, as the search for quantum gravity effects or the detection of weak stochastic forces,[4,5] to quantum technology applications. In fact, by adding an electrical degree of freedom (like an electrode) to the mechanical device, one can realize bidirectional frequency electro-optomechanical modulators to convert optical signals or ultrasensitive transducers for a shot-noise limited nuclear magnetic resonance (NMR).[6] These kinds of hybrid devices are gaining momentum in foreseen quantum networks due to their peculiar property of maintaining the quantum coherence for very long times.[7]

A wide variety of mechanical oscillators can be designed and coupled with a light field, like silicon optomechanical crystals, silica microtoroids, silicon nitride nanobeams, or nanomembranes, with masses ranging from μg to pg and frequencies from kHz to GHz.[8] In general, quantum properties of all optomechanical systems are hidden and/or destroyed by thermal noise. For this reason, all quantum effects observed to date have been obtained on resonators placed in a cryogenic environment. Unfortunately, this requirement is a major obstacle to the realization of exploitable sensors; therefore, a recent branch of research and a few recent experiments on levitated nanospheres[9–12] are progressing toward a new generation of optomechanical systems and able to maintain a quantum behavior even at room temperature. Actually, to facilitate room temperature optomechanics, two major parameters should be improved: the optomechanical cooperativity C proportional to the optomechanical interaction strength and the $Q \times \nu$ product inversely proportional to coupling between the resonator and the surrounding thermal bath. When cooperativity C is larger than the number of quanta in the mechanical resonator $n_{th} \cong k_B T/\hbar\nu$, the phonon–photon transfer is faster than the decoherence rate due to phonon leakage from the resonator to the thermal bath. Cooperativity is defined as the ratio between the square of the coherent coupling rate g and the product between the optical (κ) and mechanical (γ) dissipation rates: $C = 4g^2/(\kappa\gamma)$ where $g = g_0\sqrt{n_c}$, with n_c being the intracavity photon number and g_0 being the single-photon coupling rate. Hence, improving cooperativity means reducing losses and improving the optomechanical interaction. In turn, reducing losses improves the number of coherent oscillations the resonator can undergo before one environmental phonon enters the system, which is just the product $Q \times \nu$. If we compare this figure with the thermal decoherence rate $k_B T/(Q\hbar)$, we easily find the condition for neglecting thermal decoherence over one mechanical period, that is, $Q \times \nu > 6.2$ THz at room temperature.

Usually the resonator is embedded into a high-finesse optical Fabry–Pérot cavity, where interaction between photons and phonons takes place. The cavity is externally pumped with a monochromatic laser source (for example, a Nd:YAG IR laser), and the radiation pressure exerted by the optical field on the vibrating device generates intensity cavity field fluctuations containing information about its displacement. This technique has been used to probe a wide variety of physical phenomena.[8] In the classical domain, we have studied parametric squeezing of mechanical motion induced by optical field modulation,[13] while in the quantum domain, we have harnessed the optomechanical interaction to make a quantum non-demolition measurements of optical fields,[3] and more recently, we explored the border between the classical and quantum physics by observing the quantum signature of a squeezed mechanical oscillator.[14]

In this work, we focus on resonators based on stoichiometric Si_3N_4 membranes, commonly used in optomechanical setups. Here, to comply with the requirement $Q \times \nu > 6.2$ THz, needed for room temperature cavity optomechanics, the membrane is tensioned to dilute mechanical dissipation in a scheme first proposed in the mirror suspensions of gravitational wave antennae.[15] Thanks to this effect, nanobeams or nanomembranes made of thin nitride amorphous films, with intrinsic Q-factor of 4000, can reach ultra-high Q-factors of the order of 10^8 to 10^9 if produced with an internal stress of about 1 GPa.[16,17] However, the dilution of dissipation is a design strategy that can be exploited also in other materials and can be complemented by other strain engineering approaches. For instance, in III–V semiconductors (GaAs, GaNAs, and $In_{1-x}Ga_xP$), strain tunability is obtained by lattice mismatch between the films epitaxially grown and the substrate, and also in this case, the resulting tensile stress can exceed 1 GPa.[18] In the following, we compare the performances of two state-of-the-art designs for membrane resonators, considering the stress engineering framework, the fabrication issues, and their ultimate performances in view of room temperature optomechanic applications. We set out design rules that we plan to use in developing future ultra-high coherence devices.

II. DAMPING ANALYSIS

The total mechanical dissipation can be obtained as the incoherent sum of extrinsic (for instance, gas damping and clamping losses) and internal contributions. Internal losses can be classified into following categories: intrinsic dissipation originated from the delay between strain and stress in the material, thermoelastic loss with local heat generation and conduction, and Akhiezer damping due to coupling between the strain field and phonon modes. In devices based on Si_3N_4 membranes, the intrinsic dissipation determines the ultimate sensitivity of the device, as thermoelastic and Akhiezer losses are at least one order of magnitude lower then the intrinsic losses in the case of silicon nitride.[19] Clamping losses are also negligible in the considered devices, thanks to the use of on-chip seismic filtering stage or phononic bandgap crystal effectively isolating the membrane from its frame.[20,21]

A. Dissipation dilution by uniform stress

A static strain ε_0 originates in a Si_3N_4 film from the mismatch between the linear expansion coefficient of the nitride layer and the

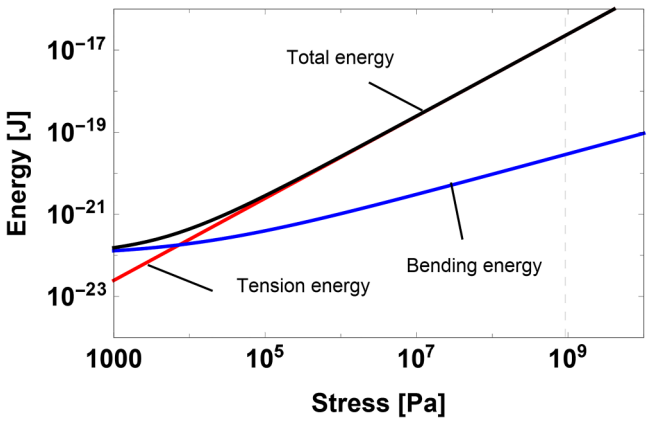

FIG. 1. Energy diagram for the (0,1) mode of a round-shaped nanomembrane resonator with dimensions $D = 1480\,\mu$m, thickness $h = 100$ nm showing the contribution of the tensile, the bending energy, and the total energies by varing internal stress σ.

substrate during the cooling phase that follows the Low Pressure Chemical Vapor Deposition (LPCVD) process. As a consequence, a biaxial state of stress σ builds up in the film and reduces intrinsic mechanical dissipation. After the first observations by Southworth,[22] this effect has been theoretically investigated for 1D or 2D micro- and nano-mechanical resonators (strings or membranes) showing that the stress "dilutes" intrinsic dissipation, thanks to the increase in the oscillator resonant frequency while bending losses remain essentially constant.[17,23] A more recent approach made clear that the Q-factor increase can be evaluated as the ratio between the total elastic energy due to internal stress σ and the bending energy,[25]

$$\frac{Q}{Q_{int}} = \frac{W_{tens}}{W_{bend-edge} + W_{bend-internal}}, \tag{1}$$

where Q_{int} is the intrinsic Q-factor (when $\sigma = 0$), and in the bending energy, we have separated the contribution from the edge to that of the internal region of the resonator. Figure 1 shows the energy balance for the fundamental mode of a 2D round-shaped membrane with dimension $D = 1480\,\mu$m and thickness $h = 100$ nm as a function of tensile stress. The energy terms in Eq. (1) are evaluated according to the formulas in Appendix A. As it is possible to fabricate films with a stress level in excess of 1 GPa, it is easy to produce a device dominated by tensile energy.

B. Edge and distributed dissipation

As pointed out by Schmid and Yu,[17,23] intrinsic dissipation can be separated in the sum of two fundamental contributions: one due to bending at the clamping edge of the membrane and the other one coming from the internal area, mainly at the antinodes where local bending is higher. The procedure for evaluating losses of a round-shaped membrane is fully described in Appendix A. The modal shape of a vibrating axisymmetric mode is decoupled into two contributions. In fact, the Bessel functions describing the simply supported circular plate is replaced, near a small annular clamping region of thickness δR (see Fig. 2), by the modal shape of

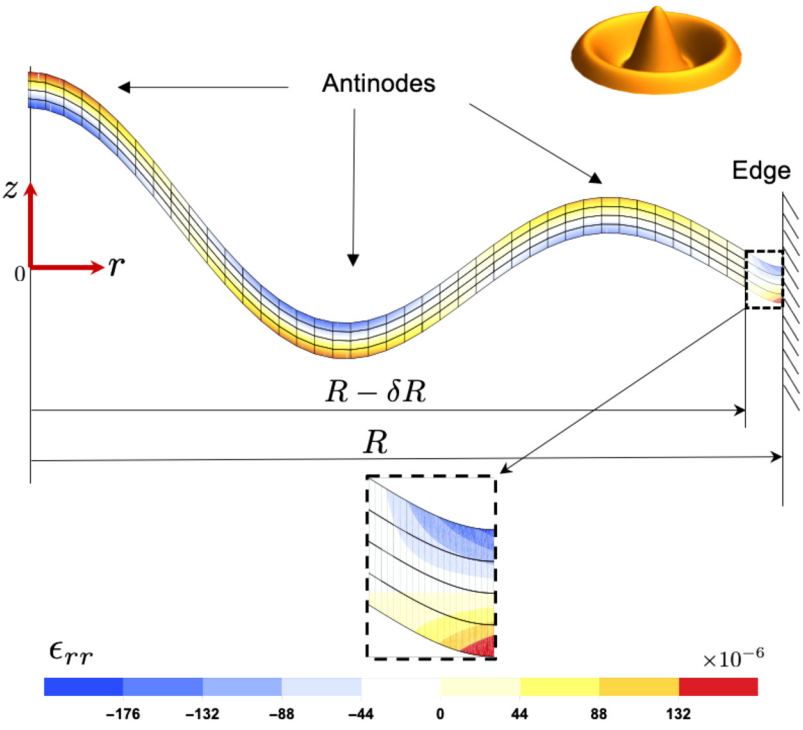

FIG. 2. Cross section of a round-shaped membrane showing the radial bending strain (ϵ_{rr}) countour plot in the case of an axisymmetric mode (0,3) for a modal amplitude of 500 nm. Antinodes strain (distributed loss) in the region $(0, R - \delta R)$ and edge strain (edge loss) in the region $(R - \delta R, R)$ (not in scale) are shown.

a round-shaped membrane under circumferential tension acting on radius $R - \delta R$ and with a clamped edge boundary condition (see Appendix A). Figure 2 shows the bending radial strain ε_{rr} calculated with a displacement amplitude of 500 nm (see Appendix B). Concentration of the strain can be seen at the antinodes and in the small region close to the edge. In Fig. 3, the Q-factor is evaluated with Eq. (1). We point out that edge dissipation is frequency independent, while distributed loss contribution increases with the modal index. Analytical approaches for evaluating the total intrinsic loss were first developed for 1D doubly clamped beams and then extended to 2D nanomembranes,[23] while a general approach for numerically estimating intrinsic dissipation of 3D structures is discussed by Fedorov.[25] In the anelastic loss model, the stress σ is delayed with respect to strain ε: $\sigma = (Y + i\phi Y)\varepsilon$, where the loss angle is related to the Q-factor as $\phi = Q^{-1}$ and Y is the Young modulus. To clarify the role of edge dissipation in the total loss budget, we focus on the curvature in the case of 1D tensioned doubly clamped nanostring of length L, thickness h, and width w,

$$YI_z \frac{d^4 u_n}{dx^4} - \sigma_0 hw \frac{d^2 u_n}{dx^2} - \rho_l \omega_n^2 u_n = 0, \tag{2}$$

where $YI_z = \frac{Yh^3 w}{12}$ is flexural rigidity, u_n is the modal shape function, σ_0 is the internal stress, and $\rho_l = \rho hw$ is the linear mass density. At the clamping point, the inertial term $\rho_l \omega_n^2 u_n$ is negligible, and the mean curvature at the edge can be approximated as

$$\frac{d^2 u_{cl,n}(x)}{dx^2} = \left(\frac{du_n}{dx}\right)_{x=+0} \frac{1}{\lambda L} \exp\left(-\frac{x}{\lambda L}\right), \tag{3}$$

where $\lambda = \sqrt{1/12\varepsilon_0}\, h/L$ is known as the dilution factor, essentially the ratio between bending and elongation energies. From Eq. (3), the shape function at the clamping edge experiences sharp exponential bending. The derivative $du_n/dx(0+)$ cannot be zero, because far from the clamping points the bending term can be neglected, and the solution to Eq. (2) has a sinusoidal shape, which has to be connected with the solution at clamping $u_{cl,n}$ containing the exponential term. In the high-strain limit, we have $\lambda \ll 1$ in both string and membranes, and the critical region close to the clamping edges can be estimated as $L_{cl} = \sqrt{Y/(12\sigma_0)}h \approx 5h = 500$ nm for h = 100 nm. Therefore, the edge loss involves only a small region where major dissipation takes place. The procedure described above can be extended to 3D square membrane of side L by solving the general equation for vibrational plates written in terms of adimensional coordinates (η, χ),

$$\lambda^2 \nabla^4_{\eta,\chi} w_{nm} - \nabla^2_{\eta,\chi} w_{nm} - \Omega^2 w_{nm} = 0, \tag{4}$$

where w_{nm} represents the displacement in the direction orthogonal to the membrane's plane, Ω represents the normalized frequency, and $\lambda^2 = D/(\sigma_0 hL^2)$ is still the dilution parameter, now expressed in terms of the flexural rigidity of plate D. From Eq. (4), the Q-factor has been derived for a square-shaped membrane as the sum of the edge and distributed contributions,[23]

$$\frac{Q}{Q_{int}} = (2\lambda + (n^2 + m^2)\pi^2\lambda^2)^{-1}, \tag{5}$$

where Q_{int} is the intrinsic Q-factor (without dilution effect), and n and m arethe modal indexes. In Secs. II C and II D, we analyze and discuss the interplay between these two dissipation mechanisms for the two devices presented in this work.

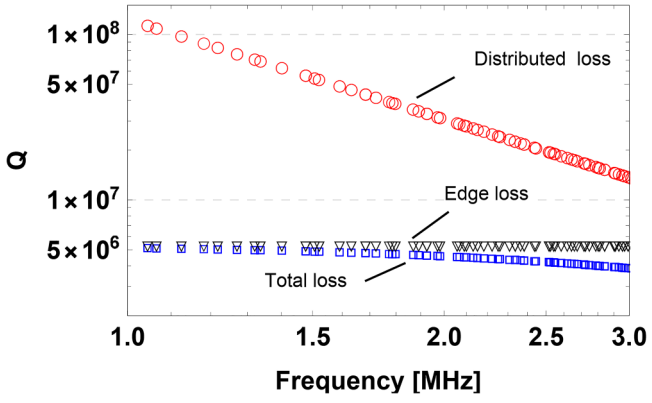

FIG. 3. Expected Q-factor for a round-shaped membrane (dimensions $D = 1480\,\mu$m, thickness $h = 100$ nm, and $\sigma = 0.918$ GPa) when edge (black triangles), distributed (red circles), or total loss (blue squares) contributions are considered.

C. Round-shaped membranes and modal expansion

In the case of a round-shaped membrane of radius R, the solutions to Eq. (4) are the Bessel functions J_m,

$$w_{mn}(r, \theta) = k_{mn} J_m\left(\alpha_{mn} \frac{r}{R}\right) \cos(m\theta), \tag{6}$$

where (r, θ) is the cylindrical coordinate system centered in the membrane with $\mathbf{i_z}$ aligned along the membrane's out-of-plane axis. α_{mn} is the nth root of the Bessel polynomial of order m. The constant k_{mn} is fixed by the normalization requirement,

$$h \int_S dS \rho w^2_{mn}(r, \theta) = M \tag{7}$$

as

$$k_{mn} = \sqrt{\frac{\pi R^2}{\int_S dS J_m^2(\alpha_{mn} \frac{r}{R}) \cos^2(m\theta)}}, \tag{8}$$

where h is the membrane's thickness and M is its mass. In the context of the modal expansion theory,[24] spatial variables can be separated from the temporal ones. Therefore, the displacement of the membrane $u(r, \theta, t)$ can be written as a superposition of normal modes with time-dependent coefficients,

$$u(r, \theta, t) = \sum_{mn} a_{mn}(t)\, w_{mn}(r, \theta). \tag{9}$$

The membrane is then sampled on its surface by a readout with output X,

$$X(t) = \int_S dS\, P_s(r, \theta)\, u(r, \theta, t), \tag{10}$$

where P_s is the weight function of the readout, normalized such that $\int_S dS\, P_s(r, \theta) = 1$ and depending on the measurement technology adopted. For instance, an optical readout based on the laser beam is sensitive to the position of the membrane's surface, averaged over the Gaussian beam profile with a waist w_0,

$$P_s(r, \theta) = \frac{2}{\pi w_0^2} e^{-2r^2/w_0^2} \equiv \frac{2}{\pi w_0^2} e^{-2(x^2+y^2)/w_0^2}. \tag{11}$$

The normalization choice Eq. (7) allows the convenient way of describing the motion of each mode w_{mn} as harmonic oscillation with effective mass,

$$m_{mn}^{\text{eff}} = \frac{M}{\left(\int_S dS\, P_s(r, \theta)\, w_{mn}(r, \theta)\right)^2}. \tag{12}$$

From this equation, it is easy to see that the lowest value of the effective mass is obtained when the readout samples a region of maximum oscillation amplitude (anti-node), while m_{mn}^{eff} increases if the readout samples a nodal region. For $(0, n)$ axisymmetrical modes read by a laser beam centered on the membrane axis, the effective mass is

$$m_{0n}^{\text{eff}} = \frac{M J_1^2(\alpha_{0n})}{\left(2\pi \int_0^R P_s(r) J_0(\alpha_{0n} \frac{r}{R}) r dr\right)^2}, \tag{13}$$

where $M = \pi R^2 h \rho$ is the membrane physical mass, $J_0 and J_1$ are the two lowest order Bessel functions, and α_{0n} is the nth root of J_0. We remind that, in the pair of indexes (m, n), the index m is the number of radial nodal lines and n is the number of circumferential nodal lines. In the lowest frequency drum mode (0,1), the circumferential node is the fixed edge. If the waist of the laser is much smaller than the membrane's radius, the first values of m_{0n}^{eff}/M are 0.269, 0.116, 0.074, and 0.054. We note that the effective mass of the drum mode (0,1) is about 1/3 of the total membrane's mass.

D. Soft-clamped rectangular membranes

An effective method to reduce edge loss is to localize the vibrational modes away from the clamping region by soft-clamping. In this way, we achieve a clamping-free device where edge losses can be neglected. Soft-clamping is a novel design strategy based on phononic crystals proposed by Tsaturyan in the case of a square-shaped membrane[21] and then applied to nanostrings.[25,26] The bandgap of the phononic crystal is matched to the resonant frequency of the so-called "defect modes" in the central part of the phononic structure (Figs. 4 and 5). A defect mode evanescently couples to the frame, therefore eliminating the extra curvature at the edge imposed by boundary conditions. Figure 5 shows that the effectiveness of this soft-clamping depends on the number of phononic cells on the device: for instance, with nine cells, the displacement at the edge is reduced at least a factor of 100 with respect to the center of the defect region. The Q-factor is limited only by distributed losses when the edge contribution of the bending energy is neglected in Eq. (1). As a consequence, Q-factors in the bandgap region reach values in excess of 10^8. Outside the bandgap, the Q-factor of modes drop and is still limited by edge losses.

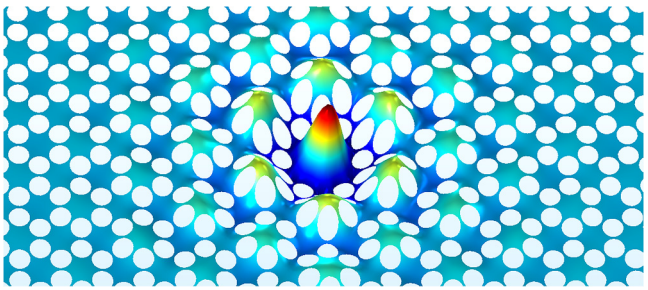

FIG. 4. Modal shape function of a bandgap mode A evaluated by a 3D finite element simulation.

For a 1D string resonator of thickness h, Eq. (1) for the mode u_n is

$$\begin{aligned} Q &= Q_{int} \frac{W_{tens}}{W_{bend-internal}} \\ &= Q_{int} \frac{\int_0^L \sigma(x) A(x) \left(\frac{du_n(x)}{dx}\right)^2 dx}{\int_0^L Y I_z(x) \left(\frac{d^2 u_n(x)}{dx^2}\right)^2 dx} \\ &= \eta \beta \frac{\sigma_0}{Y} \frac{a^2}{h}, \end{aligned} \tag{14}$$

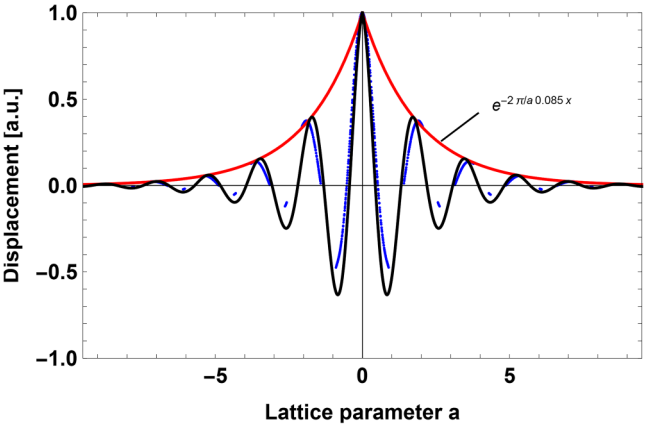

FIG. 5. The bandgap mode A cross section along x axis. Blue curve is derived by the FEM modal analysis, the red curve is an exponential function as a guide to the eye, and the black is the sinusoidal decaying approximation, showing the evanescent decay.

where σ_0 is the average stress, $A(x) = h(x)w$ is the cross section area, a is the lattice parameter, L is the string length, η is a prefactor related to the mode shape, and β is the average surface loss parameter. We point out that in this equation, the intrinsic dissipation contribution is mainly due to surface losses $Q_{int}^{-1} = \frac{1}{\beta h}$. In fact, surface loss is one of the damping mechanisms in micro- and nano-mechanical nitride resonators, and its contribution dominates when the thickness h is less than 100 nm.[27]

For a nanomembrane, the analogous of Eq. (14) becomes

$$\begin{aligned} Q &= Q_{int}\frac{W_{tens}}{W_{bend-internal}} \\ &= Q_{int}\frac{h\int_{-L_1/2}^{L_1/2}\int_{-L_2/2}^{L_2/2}\sigma(x,y)\left(\left(\frac{\partial w_{BG}(x,y)}{\partial x}\right)^2+\left(\frac{\partial w_{BG}(x,y)}{\partial y}\right)^2\right)dxdy}{D_z\int_{-L_1/2}^{L_1/2}\int_{-L_2/2}^{L_2/2}\left(\frac{\partial^2 w_{BG}(x,y)}{\partial x^2}+\frac{\partial^2 w_{BG}(x,y)}{\partial y^2}\right)^2 dxdy} \\ &= f(a)\times\frac{\sigma_0}{Y\,h^2}\times\frac{1}{\phi+\frac{1}{\beta h}}, \end{aligned} \tag{15}$$

where w_{BG} is the modal shape function of a defect mode and $f(a)$ is numerically evaluated from the mode shape as a function of lattice constant a and of the membrane size. In this case, bulk loss parameter ϕ and surface loss parameter β concur to determine the overall dissipation of the mode. For a membrane with dimensions $L_1 = 19\,a$ and $L_2 = 19.5\,a$, the shape of the bandgap mode A is

$$\begin{aligned} w_A(x,y) = k_A e^{(-2\pi/a\ 0.085\ (|x|+|y|))} \\ \times\cos(2\pi/a\ 0.57\ |x|)\cos(2\pi/a\ 0.57\ |y|), \end{aligned} \tag{16}$$

where k_A is determined by the normalization requirement [Eq. (7)]. This shape function is compared in Fig. 4 with FEM evaluation. The effective modal mass for mode A can be estimated by numerically evaluating the eigenfunction by finite elements or from the modal shape $w_A(x,y)$ as

$$m_A^{\text{eff}} = \frac{M}{\left(\int_{-L_1/2}^{L_1/2}\int_{-L_2/2}^{L_2/2} P_s(x,y)\,w_i(x,y)\,dxdy\right)^2}. \tag{17}$$

III. CHIP-SCALE OPTOMECHANICAL Si_3N_4 OSCILLATORS

In the following, we describe the fabrication of a round-shaped nanomembrane with an on-chip isolation stage[20,28] and a rectangular-shaped geometry endowed with a phononic bandgap structure,[21] both designed and produced in our microfabrication facility. The former is produced by bulk/surface micromachining using Deep-RIE and its quality factor is mainly limited by edge losses, while the latter is produced by wet anisotropic KOH etching and is limited by distributed losses. Both membranes have an intrinsic stress of the order of 1 GPa, have a dilution factor in the range of $\lambda \simeq 10^{-4}$, and feature a number of low loss mechanical modes resonating at frequencies in the MHz range with a modal effective mass in the range of pg to ng.

A. Round-shaped membrane with an on-chip shield

Tensioned round-shaped membranes were produced with a uniform stress $\sigma_0 = 0.918 \pm 0.02$ GPa. The filtering structure shown in Fig. 6 was patterned on a 1 ± 0.025 mm thick Silicon-On-Insulator (SOI) wafer with a Deep-RIE silicon etching Bosch process. We exploit the $2\,\mu$m thick buried oxide as an etch stop layer when patterning the spring structure on the front side and the masses in the back side of the wafer. Additional metallic and dielectric sacrificial layers were used during processing to protect devices from scratching and from chemicals. All structures are patterned using contact aligner lithography and hard-contact exposure in the back side of the wafer. The membrane radius is defined by the re-entrant sidewall slopes of successive Deep-RIE steps that enlarge the central hole patterned using lithography. Depending on the details of the etching procedure, diameter in the range of $1500 \pm 150\,\mu$m can be obtained. In order to evaluate possible effects of edge dissipation on Q, we fabricated devices with two clamping conditions: membrane directly pinned to the silicon substrate (stitched membranes) and membrane without contact with the substrate. To this aim, two oxides were used as sacrificial layers for the Deep-RIE last etching step: the LPCVD TEOS oxide shown in Fig. 6 (top) and the thermally grown oxide shown in Fig. 6 (bottom). In both cases, the sacrificial oxide layer underneath the membrane was removed with an HF aqueous solutions and then rinsed with de-ionized water. Stitching is obtained by undercutting the LPCVD buried oxide below the edges of the window as demonstrated by Gopalakrishnan.[29] Figure 7 shows, in the case of non-stitched membrane, the initial undercut produced by HF etching of the oxide layer between the membrane and the substrate. The cross section of the profile is irregular and wave-like but at a scale of hundreds of nanometers with respect to millimeter scale of membrane's radius. Given the relatively large etching rate of LPCVD oxide, about three times greater than the thermally grown oxide, it is possible to obtain undercuts extending for $0.6–3\,\mu$m underneath the membrane. Membrane's stitching happens when the capillary forces of liquid trapped in the undercut region overcome the bending rigidity of the membrane. The undercut depth is observed to grow approximately linearly with etch time, and we found that the minimum length to promote stitching is $0.6\,\mu$m. Smoothness of the contact surfaces influences the edge losses and the presence of polymer residues from the Deep-RIE process. To ensure repeatability over a number of devices and reduce edge loss, we made aggressive oxygen plasma steps after the last Deep-RIE step and flux DI water onto the membrane's edge after the HF release step.[30]

B. Rectangular shaped membrane with phononic bandgap

The device was fabricated with a customized version of the process described in Tsaturyan.[21] Two PECVD oxide and nitride extra-layers are used to balance and protect the high stress SiN membrane with the aim to increase the process yield. The thickness and the stress are the same to the one used for the circular shaped membrane: 100 nm thick and $\sigma_0 = 0.918 \pm 0.02$ GPa, respectively. The silicon frame is $14 \times 14\,\text{mm}^2$ in order to mantain the same mounting apparatus used for the round-shaped membranes. Details of the soft-clamped membrane are shown in Fig. 8. The intrinsic stress and

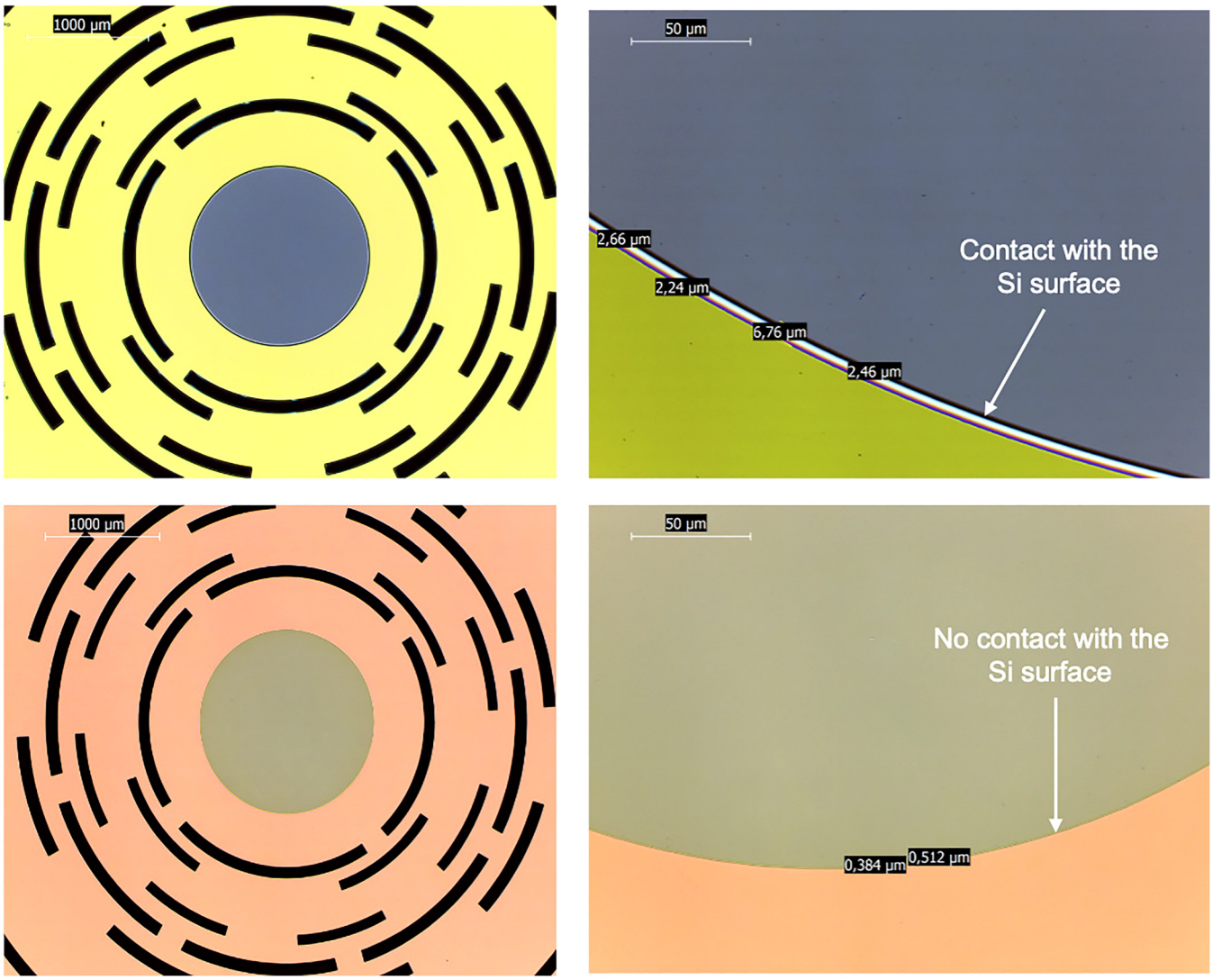

FIG. 6. Round-shaped Si_3N_4 membrane surrounded by the on-chip filter and a detailed view of the membrane's edge. (Top) Case of Si_3N_4 deposited on a LPCVD TEOS oxide sacrificial layer where the membrane is stitched on the Si substrate. (Bottom) Case of Si_3N_4 deposited on a thermally grown oxide without membrane's stitching to the substrate.

the thickness are constant while we built devices with the lattice parameter $a = (160, 346, 360, 380)\,\mu$m, with corresponding overall membrane size $19\,a \times 19.5\,a$. Devices were fabricated on a double-side polished 0.525 ± 0.015 mm thick wafer with roughness of 0.5 nm RMS. The tensioned LPCVD stoichiometric Si_3N_4 layer, with stress tuned to 0.918 ± 0.02 GPa, was covered with $4\,\mu$m resist to pattern the phononic bandgap lattice by UV lithography in hard contact mode. The silicon nitride layer is then etched with fluorine-based plasma. Note that the Si_3N_4 layer is grown directly on the silicon surface without an oxide sacrificial layer as in the case of a round-shaped device. The bulk micromachining was done by KOH etching using a 35% KOH at 80 °C to get a reasonable and constant etching rate, that is critical for an optimal release of membranes. The sacrificial layers on the front side were removed by dry plasma and wet BHF etching. With hot DI water, we remove residues from the KOH bath and clean the membrane surface. We point out that scratches or resist imperfections before UV lithography can trigger the membrane failure during the release phase, handling, or dicing.

IV. Q-FACTOR MEASUREMENT WITH AN INTERFEROMETRIC SETUP

The mechanical properties of the devices have been characterized by a displacement sensing setup made by a polarization-

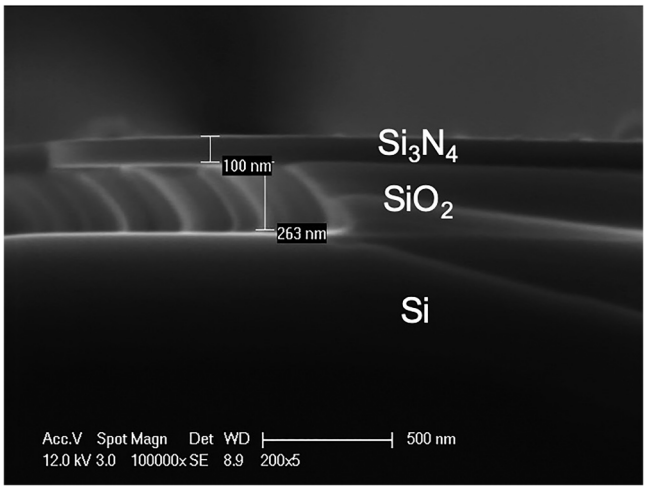

FIG. 7. SEM image at the edge of the membrane after partial breakage of a round-shaped membrane showing the undercut of the oxide supporting the thin Si_3N_4 membrane.

sensitive Michelson interferometer with displacement sensitivity of about 10^{-30} m^2/Hz, whose scheme is shown in Fig. 9, while Fig. 10 shows a detailed view of the suspension system. The laser source is a continuous wave (CW) ND:YAG laser operating at 1064 nm (Coherent-Mephisto). The laser beam is first coupled to a Faraday isolator (FI1) (the corresponding coupling optics is omitted in the figure) in order to prevent instabilities in the laser source due to back reflections, and then it is split into two parts by a polarizing beam splitter cube (PBS1). A main beam of few mW (probe beam) is sent to the interferometer through a port of the PBS, while the output from the second port is blocked by a beam dump. In this scheme, PBS1 is only used to limit the power of the probe beam. A second beam splitter (PBS2) divides the probe beam. The reference arm is focused to an electromagnetically driven mirror M_1, that is used for phase-locking the interferometer in the condition of maximum displacement sensitivity. The sensing arm is instead focused with a waist below 100 μm on the oscillator kept in a vacuum chamber at a pressure of 10^{-6} mbar. After the reflection and a double pass through a quarter-wave plate, both beams suffer a 90° rotation of their polarization, and then they are completely transmitted (reference beam) or reflected (sensing beam) by the PBS2. The overlapped beams are then monitored by homodyne detection, consisting of a half-wave plate, rotating the polarizations by 45°, and a polarizing beam splitter (PBS3) that divides the radiation into two equal parts sent to photodiodes PD1 and PD2, whose outputs are subtracted. The signal obtained is a null-average, sinusoidal function of the path difference in the interferometer. Such a scheme is barely sensitive to laser power fluctuations. The difference signal is used as an error signal in the locking servo-loop (the locking bandwidth is about 300 Hz) and also sent to the acquisition and measurement instruments. In order to measure the Q-factor, we first drive the system at resonance frequency ν_m by a piezoelectric actuator mounted on the sample holder, and then remove the drive and acquire the amplitude of the displacement signal using the interferometer. The mechanical vibration follows an exponentially damped decay whose envelope amplitude varies according to $u(t) = u_0 \exp(-t/t_m)$, where $t_m = Q/(\pi\nu_m)$ is the decay time of the mode.

V. MEMBRANE INSIDE AN OPTICAL CAVITY

The use of membrane oscillators in high sensitivity optomechanical nanosensors implies that they should be located inside high Finesse optical cavities, as partially reflecting surfaces. As a

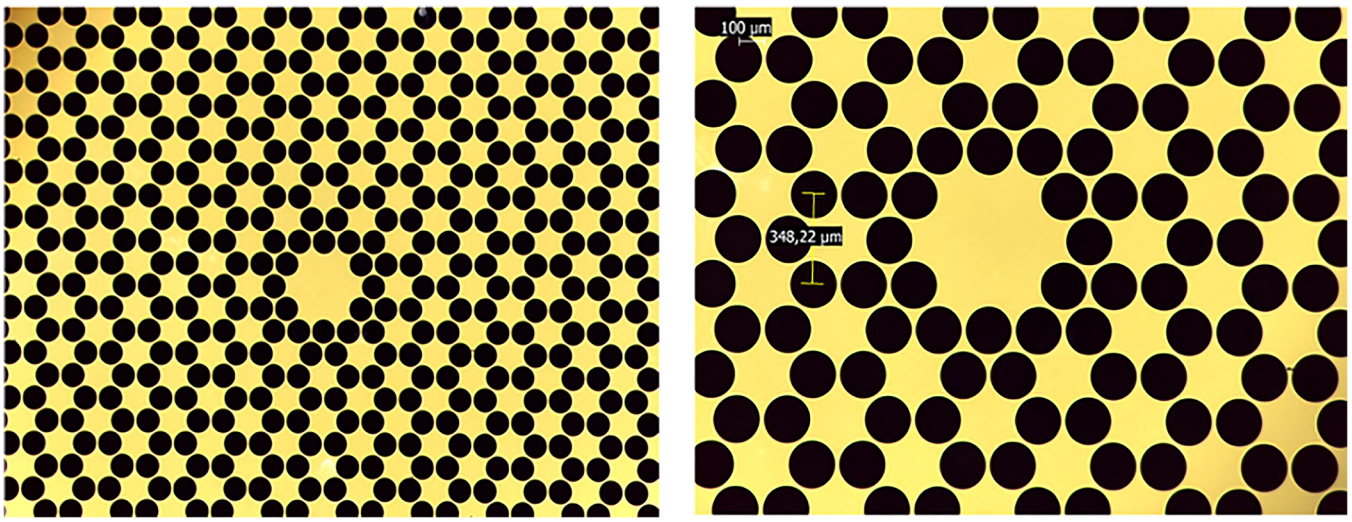

FIG. 8. Phononic bandgap lattice (a = 346 μm) (left) with a detailed view of the central resonating part (right) with the hexagonal-shaped defect region in the center of the lattice.

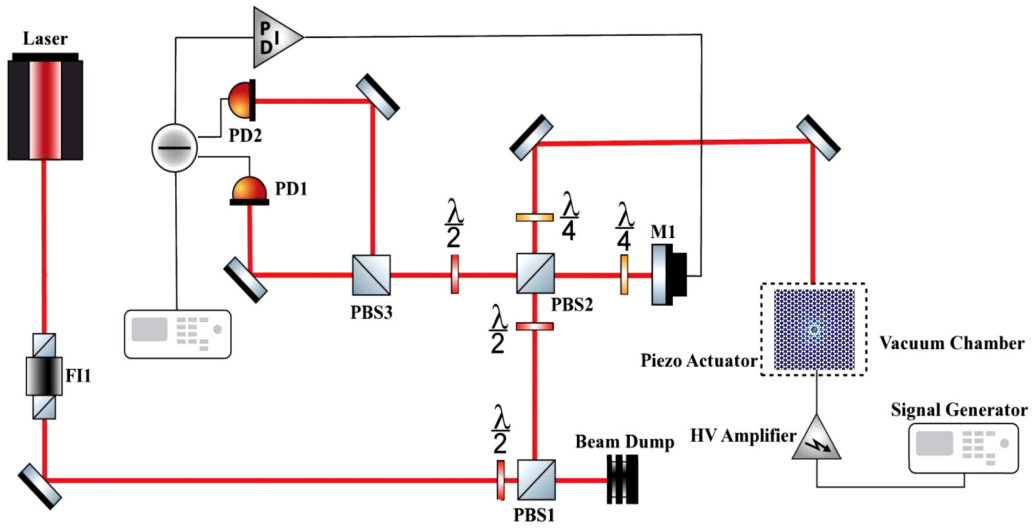

FIG. 9. High-sensitivity interferometer scheme for Q-factor measurements.

consequence, they should not spoil the cavity optical quality, and their overall mechanical noise (including the sensing mode and all the other mechanical modes) should be low enough to allow a stable frequency locking between the cavity optical resonance and the laser field. In order to test these requirements, we have mounted the dices incorporating the membranes inside plano-concave cavities using silicon spacers between the membrane dice and the flat mirror to guarantee parallelism and mechanical stability. The round membranes with acoustic shield have been successfully used even inside helium flux cryostats in quantum optomechanics experiments.[10,31–33] Concerning the rectangular membranes with a phononic bandgap structure, we have tested the PM-360 sample inside a 48 mm long cavity in high vacuum at room temperature. We show in Fig. 11 the Pound–Drever–Hall signal obtained in this setup by phase modulating the probe laser at 13.3 MHz. The fit to the data gives a cavity linewidth of 250 kHz (Finesse 12000), setting the bandgap modes in the resolved sidebands regime, with optical losses dominated by input mirror transmission. The laser was then stably locked to the cavity. In the inset of Fig. 11, we show a portion of the spectrum of the same Pound–Drever–Hall signal, exhibiting the resonance of the A mode, slightly optically cooled by an additional weak, red-detuned beam.

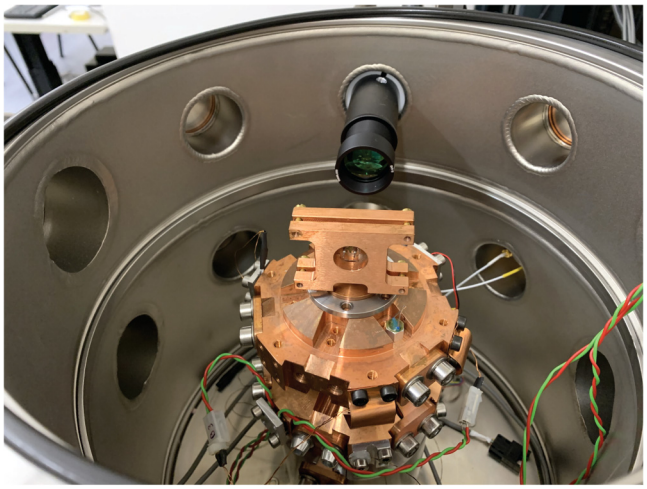

FIG. 10. Detailed view of the OFHC copper support for the resonators with the filtering suspension system clamped at the bottom of the vacuum chamber.

VI. RESULTS AND DISCUSSION

In this section, we compare the performances of the two optomechanical sensors in terms of $Q \times \nu$ product and force sensitivity. We discuss advantages and drawbacks also in terms of modal density, surface's functionalization, and microfabrication process complexity.

A. Figure of merit $Q \times \nu$

In round-shaped membranes, modal frequencies are calculated by the well-known analytical formula: $\nu_{nm} = \frac{1}{\pi 2R}\alpha_{nm}\sqrt{\frac{\sigma}{\rho}}$, where α_{nm} is the root of the Bessel function J_m and (n, m) are the radial and circumferential modal indexes. For rectangular membranes with a phononic crystal, the modal frequencies are numerically evaluated by Finite Element Analysis (FEA). The modal shapes of the five out-of-plane modes in the bandgap are shown in Fig. 12, where the first mode A is a singlet while (B, C) and (D, E) are doublets. Similar to what shown for mode A in Fig. 4, all bandgap modes are well localized in the defect region and the displacement of the membrane fades out by going toward the edge, thus achieving the soft-clamping condition. In Figs. 13 and 14, we compare

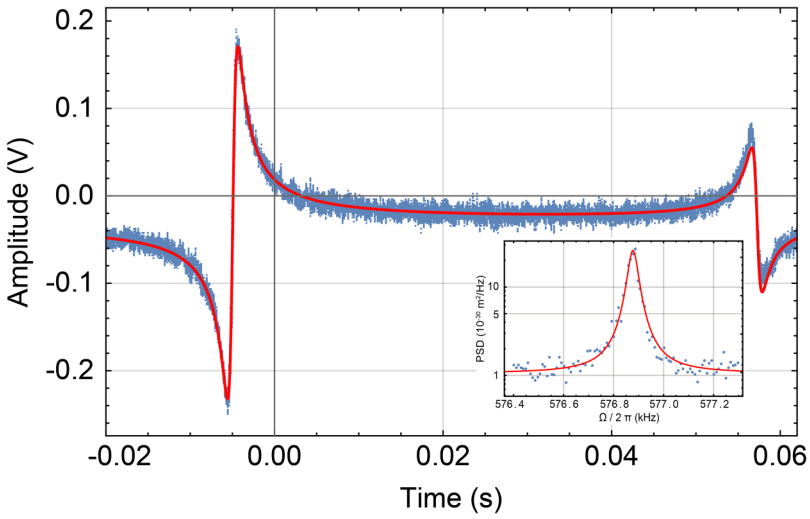

FIG. 11. Pound–Drever–Hall signal from an optical cavity containing a membrane with phononic bandgap structure. The distance between the carrier (left dispersive signal) and the sideband (right signal) is 13.3 MHz and is used to calibrate the frequency scan. Inset: power spectral density (PSD) of the A mode.

the Power Spectral Density (PSD) of the displacement of the central area of the devices, measured for acoustic frequencies up to 2 MHz. Here, the modes are driven by the thermal force to an amplitude depending upon the modal equivalent mass and upon coupling with the laser beam. In the case of the round-shaped membrane, the normal modes are well separated and emerge from the background noise of 10^{-30} m^2/Hz (Fig. 13). In general almost all expected modes can be found at the expected modal frequency; in the figure, we show, for instance, the position of the first drum mode (n,m)=(0,1). Here, the filtering stage effectively decouples the frame from the membrane, as described by Borrielli;[20] hence, the clamping losses are made negligible and the membrane dynamics is dominated by intrinsic dissipation, both at the clamping edge and in the central area, for all mechanical modes. The Q factor is in the range between 5 and 10×10^6, and no differences could be appreciated in the case of stitched and non-stitched membranes.

The rectangular-shaped membrane PSD spectrum, shown in Fig. 14, has a bandgap region with some distinct peaks emerging from the background noise (here at a level of 10^{-27} to 10^{-28} m^2/Hz), each corresponding to out-of-plane modes (A, B, C, D, and E). In this case, the Q-factor can be as high as 5×10^7 and scales down quadratically with the lattice constant a. In the region outside the bandgap, the modal density dramatically increases due to a large number of resonances of the phononic crystal.

For bandgap modes, we observed a dispersion of Q value in agreement with results obtained by Tsaturyan.[21] In Table I, we report the results for two rectangular-shaped membranes with lattice constant $a = 160\,\mu$m and $a = 360\,\mu$m. The performances of the devices presented in this work are fully consistent with those presented by Tsaturyan[21] if the physical parameters of the membranes are properly scaled according to the theory presented in Sec. II D,

$$\nu = \hat{\nu} \times \frac{\hat{a}}{a}\sqrt{\frac{\sigma}{\hat{\sigma}}}, \quad Q = \hat{Q} \times \frac{\sigma \hat{h} a^2}{\hat{\sigma} h \hat{a}^2}, \tag{18}$$

where the parameters (ν, Q, h, a, σ) and $(\hat{\nu}, \hat{Q}, \hat{h}, \hat{a}, \hat{\sigma})$ identify two different geometrical configurations of the device. Some interesting considerations can be drawn by comparing the estimates obtained from the models developed in Sec. II D with the measurements reported in Table I. Figure 15 shows a subset of quality factors for the mode A of membranes with varying size a in the interval 87–380 μm but with fixed thickness and stress. Results of two fabrication batches, the one from Tsaturyan[21] and the other described in Sec. III B, were aggregated in the same graph. In each fabrication batch, the stress and the thickness are fixed. To make data comparable, the frequency ν and the quality factor derived from Tsaturyan[21] are scaled to $\sigma_0 = 0.918$ GPa and $h = 100$ nm by using Eq. (18). In the same graph, we add the plot $Q \propto \nu^{-2}$ $(Q \propto a^2)$ that can be derived from the 2D model [Eq. (15)] with $\phi = 2.66 \times 10^{-4}$ and $\beta = 60 \times 10^9$ m^{-1}.

Bandgap modes in soft-clamped membranes for $a = 160\,\mu$m (high-frequency) and $a = 360\,\mu$m (low-frequency) are compared with those from round-shaped membranes in Fig. 16, showing $Q \times \nu$ (coherence rate) for the two devices. Devices with $Q \times \nu$ lying inside the gray area are compliant with the requirement for room temperature optomechanics,[8] $Q \times \nu > 6.2$ THz. For round-shaped modes, a fitting model (red-dashed) derived from Eq. (5) and multiplied by the frequency is shown and can be used for describing the behaviors of such resonators. Almost all modes of round-shaped membranes met the requirement of quantum transition at room temperature, apart from some low frequency modes. Bandgap modes of the rectangular-shaped membrane, where the quality factor is limited by the distributed loss mechanism, are fully compliant but show more scattered results between the different modes, at least for what observed with the devices obtained with our production process. Infact, high-Q devices might be very sensitive to surface losses due to fabrication imperfection or residues, especially when the oscillating part is small (to the size of the lattice parameter a). Similar behaviors are seen in data from supplementary material in Ref. 21. We believe that this comparison is fair because we produced, for both kind of devices, larger

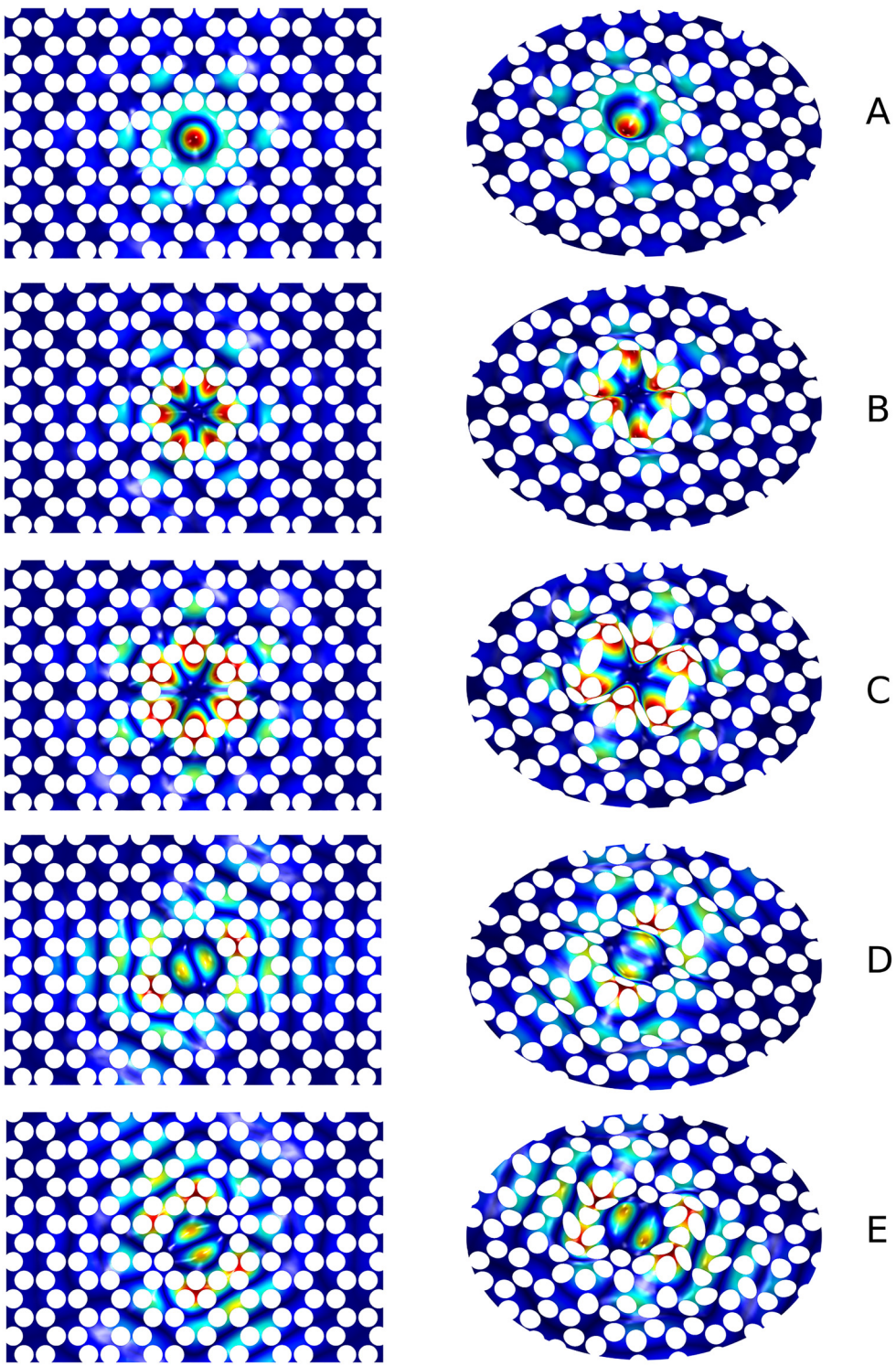

FIG. 12. FE modal analysis with $a = 160\,\mu$m of bandgap modes with frequencies $\nu_A > \nu_B > \nu_C > \nu_D > \nu_E$ showing that the defect mode evanescently couples to substrate at the edge (soft clamping). Modes B and C and D and E are doublets.

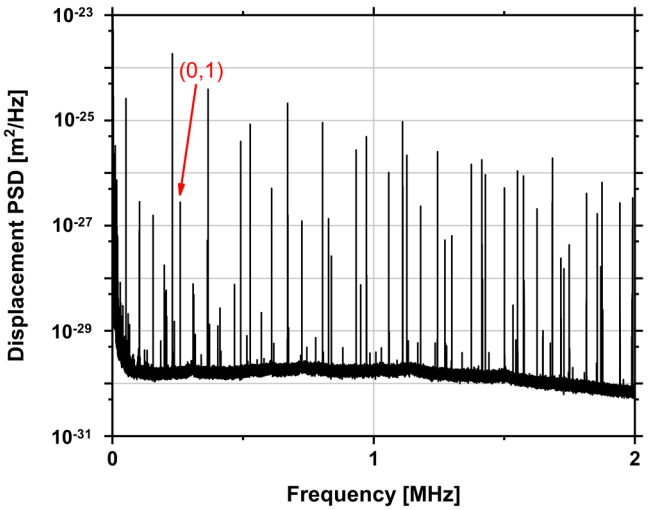

FIG. 13. Displacement PSD for the round-shaped membrane. Data are derived from the FFT of the interferometer output.

structures that could be hosted on our standard silicon frame of $14 \times 14\,\mathrm{mm}^2$.

B. Force sensitivity

The opto-mechanical membrane is an elastic body that vibrates due to the combined effects of external forces, back-action radiation pressure, and the thermal Langevin force. When the system is used as a probe for an external force, its sensitivity is limited by the equivalent input force density due to technical noises. Given that we compare devices of different geometries and sizes, the evaluation must account for the precise shape of the surface sampled by the readout and for the point of application of the external force. Here, we neglect readout backaction noise and consider only a force orthogonal to the membrane's plane and with a frequency equal to one of the membrane's resonances, say ω_n, but even the most general case could be evaluated, as done, for instance, in the context of resonant detectors of gravitational waves.[34]

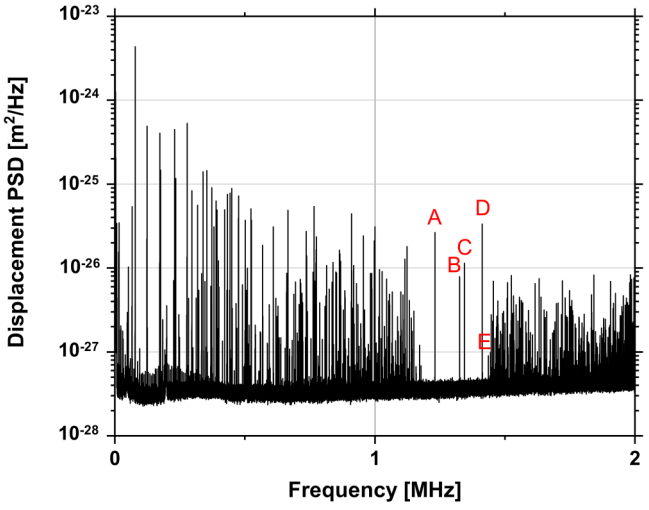

FIG. 14. Displacement PSD for a rectangular-shaped membrane with $a = 160\,\mu$m. Data are derived from the FFT of the interferometer output.

TABLE I. Measured Q-factor bandgap modes A, B, C, D, and E for square-shaped membranes with lattice constant $a = 160$ *and* $360\,\mu$m with membrane size 3040×3120 and $6840 \times 7020\,\mu\mathrm{m}^2$, respectively.

	PM-160			PM-360		
Mode	ν (MHz)	Q 10^6	$\nu \times Q$ (THz)	ν (MHz)	Q 10^6	$\nu \times Q$ (THz)
A	1.23	11.2	11.19	0.571	19.3	11.02
B	1.32	10.4	13.73	0.614	11.0	6.75
C	1.34	11.5	15.41	0.620	54.0	33.48
D	1.41	3.2	4.48	0.649	10.3	6.68
E	1.43	11.4	16.30	…	…	…

1. Generic force

Starting from normal mode expansion (9), we evaluate the displacement of the membrane when a volume force density $\mathbf{G}(\mathbf{r})$ is applied to the membrane. The total driving force comes from the integration of this force density over the volume of the membrane V. If the time evolution of the force can be separated, we write

$$\mathbf{G}(\mathbf{r}, t) = G_t(t)\, G_r(r, \theta, z)\, \mathbf{i}_z, \tag{19}$$

where $G_t(t)$ is the total force applied to the membrane and G_r is a density function describing how the force field varies in the membrane's volume, with normalization,

$$\int_V dV G_r(r, \theta, z) = 1. \tag{20}$$

Thanks to the separability of time from spatial variables, the time evolution of coefficient $a_n(t)$ is equivalent to the time development of a forced harmonic oscillator,

$$M \frac{\partial^2 a_n(t)}{\partial t^2} + M \omega_n^2\, a_n(t) = G_t(t) \int_V dV\, G_r(r, \theta, z)\, w_n(r, \theta), \tag{21}$$

where $w_n(r, \theta)$ is constant along the membrane's thickness. Note that, in order not to burden the notation, we identify the mode by a single index n in this section. In the frequency domain (here and in the following we indicate the Fourier transform with a tilda), we have then

$$\tilde{a}_n(\omega) = \frac{1}{M} \frac{\tilde{G}_t(\omega)}{(\omega_n^2 - \omega^2) + i\omega_n^2 \phi_n(\omega)} \int_V dV\, G_r(r, \theta, z)\, w_n(r, \theta), \tag{22}$$

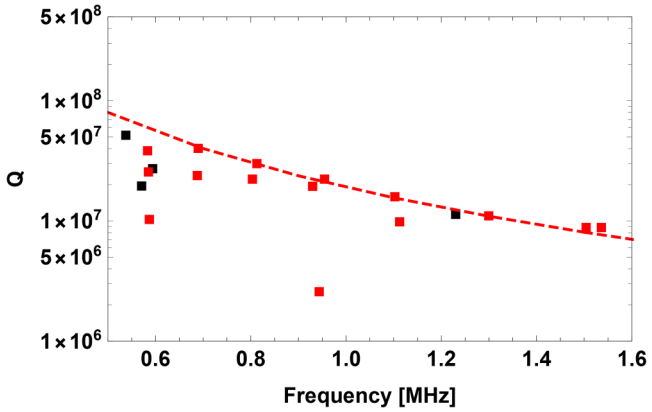

FIG. 15. Measured Q factors vs frequency for the bandgap mode A of a rectangular-shaped phononic membrane of thickness $h = 100$ nm and stress $\sigma_0 = 0.918$ GPa. Red line is the theoretical curve derived using Eq. (15) and sets a theoretical limit for the 2D phononic membrane. Data points are experimental results measured in our setup (black squares) or measured by Tsaturyan[21] (red squares). In this case, the experimental values are scaled according to Eq. (18) to allow a proper comparison when the membrane thickness or the internal stress is not the same as our devices. Dashed red line is guide to the eye, derived from Eq. (15), showing that $Q \propto \nu^{-2}$.

where the system loss is modeled in the frequency domain by including explicitly the damping term $\phi_n = 1/Q_n$.[15] If we consider the output coordinate X defined in Eq. (10), we see that, at resonance ω_m, the response $T_G(\omega) = \widetilde{X}/\widetilde{G}_t$ of the oscillator to the external force density G is

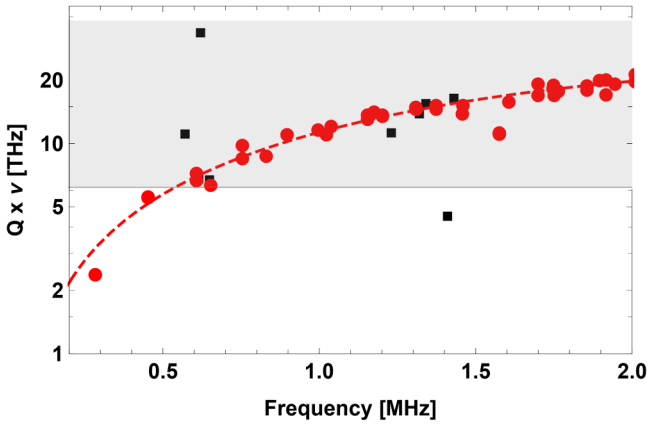

FIG. 16. The plot shows $Q \times \nu$ vs frequency for the two membranes at room temperature. Red circles refer to round-shaped membrane, and black squares refer to modes (A, B, C, and D) of soft-clamped membrane with lattice $a = 160\,\mu$m and $a = 360\,\mu$m. The red dashed line is the fitting model for the round-shaped membranes described in the Appendix C. Data points within the gray shaded area fulfill the minimum requirement for quantum optomechanics at room temperature.

$$T_G(\omega_n) = -i\,\frac{Q_n}{M\omega_n^2}\int_V dV\, G_r(r,\theta,z)\, w_n(r,\theta) \times \int_S dS\, P_s(r,\theta)\, w_n(r,\theta), \tag{23}$$

where $P_s(r,\theta)$ is the weight function of the readout, defined in Eq. (11), for an optical readout.

2. Thermal noise and sensitivity

The fluctuation–dissipation theorem states that the one-side noise PSD of the coordinate X at the angular frequency ω is

$$S_{XX}(\omega) = -\frac{4k_BT}{\omega}\,\Im\{T_F(\omega)\}, \tag{24}$$

where $T_F(\omega) = \widetilde{X}(\omega)/\widetilde{F}_t(\omega)$ is the transfer function between the readout observable X and a force F applied with the same weight function P_s of the readout,[35]

$$F(r,\theta,t) = F_t(t)\,P_s(r,\theta). \tag{25}$$

If we substitute this specific force field in the general solution Eq. (23), we find, at resonance ω_n,

$$T_F(\omega_n) = -i\,\frac{Q_n}{M\omega_n^2}\left(\int_S dS\, P_s(r,\theta)\, w_n(r,\theta)\right)^2 = -i\,\frac{Q_n}{\omega_n^2 m_n^{\text{eff}}}, \tag{26}$$

where the effective mass has been defined in Eq. (12). From Eqs. (24) and (26), the thermal noise PSD on the output variable is

$$S_{XX}(\omega_n) = 4k_BT\,\frac{Q_n}{m_n^{\text{eff}}\,\omega_n^3}, \tag{27}$$

where m_n^{eff} for the round-shaped membrane and for the gap modes of the rectangular soft-clamped membrane are evaluated, respectively, in Eqs. (13) and (17). The minimal detectable force is obtained by the comparison between the ouput X induced by the force $\mathbf{G}$ and the noise power spectral density S_{XX}. The sensitivity of the device as a detector of this force is defined as the ratio

$$S_{GG}(\omega_n) = \frac{S_{XX}(\omega)}{|T_G(\omega)|^2} \tag{28}$$

and should be as low as possible in the frequency range of interest. At resonance ω_n, we can substitute Eqs. (26) and (27) and obtain

$$S_{GG}(\omega) = 4k_BT\,\frac{\omega_n}{Q_n}\,\frac{M}{\left(\int_V dV\, G_r(r,\theta,z)\, w_n(r,\theta)\right)^2} \tag{29}$$

that make clear the role of the modal shape on the sensitivity of the system. It is not surprising that low temperatures and high-quality factors are of benefit to the measure, while the term depending on the modal shape is sometimes overlooked.

3. Point force

To study the case of a force applied in the center of the membrane, we assume for simplicity that it is directed along the membrane axis $\mathbf{i}_z$ and applied onto the surface $z = 0$ with the shape of the readout weight function $P_s(r, \theta)$. The correspondent force density is $\mathbf{U}(\mathbf{r}, t) = U_t(t)P_s(r, \theta)\,\delta(z)\,\mathbf{i}_z$, where $U(t)$ is the total applied force. The normalization of the density function is a consequence of the normalization of the weight function P_s. In this case, Eq. (29) can be rewritten as

$$S_{UU}(\omega_n) = 4k_BT\frac{\omega_n}{Q_n}\frac{M}{\left(\int_S dS\,P_s(r,\theta)\,w_n(r,\theta)\right)^2} = 4k_BT\frac{\omega_n}{Q_n}m_n^{\text{eff}}. \quad (30)$$

The sensitivity of both devices is reported in Table II, where the results have also been extrapolated to cryogenic (T = 4.2 K) and ultracryogenic (T = 14 mK) temperatures. We have extrapolated from literature data the temperature dependence of the Q-factor for soft-clamped membranes.[21] On the contrary, we have assumed a constant value of Q for round-shaped membranes.[20] Soft-clamped membranes are in general more sensitive, thanks to their higher quality factor, but in both cases, these figures outperform the pN sensitivities typical of atomic force microscopes and push us to further improve the performance and stability of the production process.

4. Uniform force field

We consider now the sensitivity of the membranes under a uniform force density field that is oriented along the membrane axis, $\mathbf{i}_z$. In this case, we have the term $G_r(r, \theta, z) = 1/V$, and Eq. (29) becomes

$$S_{GG}(\omega) = 4k_BT\frac{\omega_n}{Q_n}\frac{M\,V^2}{\left(\int_V dV\;w_n(r,\theta)\right)^2}, \quad (31)$$

where $\omega_n and Q_n$ have been measured, while the mass term is calculated by FEM using the normalized shape functions of the modal analysis. We report in Fig. 17 the sensitivity for the bandgap modes of a soft-clamped membrane produced in our facility and the sensitivity of the axisymmetric modes $(0, n)$ of the round-shaped membrane. We also add to the figure the predictions for the ultra-high Q soft-clamped membrane described by Tsaturyan,[21] featuring Q factors well over 10^7.

TABLE II. Thermal noise limits to the sensitivity to a point force at room, cryogenic, and ultra-cryogenic temperatures. RS-M: mode (0,1) of round-shaped membrane resonator. PM-*a*: mode A of the soft-clamped membrane with lattice parameter *a*. The laser waist w_0 of the readout and the effective mass of the oscillator are reported in the table. The physical parameters of the devices are listed here. RS-M: $h = 100$ nm, $f = 284$ kHz, *and* $Q = 8.7 \times 10^6$; PM-160: $h = 100$ nm, $f = 1.23$ MHz, *and* $Q = 9.1 \times 10^6$; PM-346: $h = 100$ nm, $f = 630$ kHz, *and* $Q = 19.3 \times 10^6$.

$S_{UU}^{1/2}$	$w_0\ (\mu m)$	$m_{eff}\ (ng)$	@ 300 (K) $(aN/\sqrt{Hz})$	@ 4.2 (K) $(aN/\sqrt{Hz})$	@ 14 (mK) $(aN/\sqrt{Hz})$
RS-M	600	326	1014.13	119.98	6.92
RS-M	150	132	645.42	76.37	4.41
RS-M	50	125	627.85	74.29	4.28
PM-160	50	14.7	438.41	32.81	0.96
PM-346	50	38.0	329.51	24.61	0.72

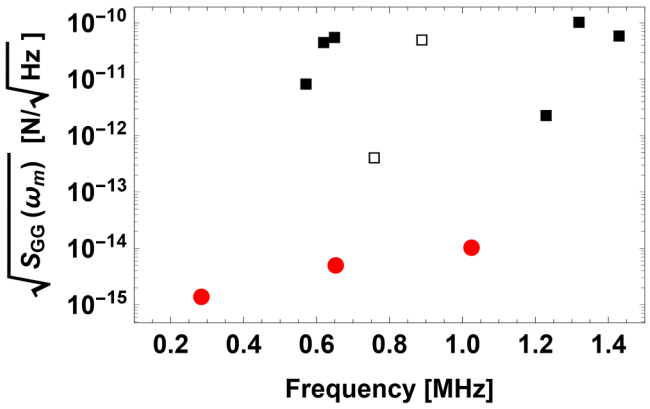

FIG. 17. Sensitivity $S_{GG}(\omega_m)$ in the case of uniform force field at 300 K. Red circles correspond to the lowest frequency axisymmetric modes of the round-shaped membrane, while black squares correspond to bandgap modes A, B, C, D, and E of the soft-clamped membrane. The empty black square refers to the soft-clamped membrane with $a = 346\,\mu$m and thickness of 35 nm described by Tsaturyan.[21]

In general, round-shaped membranes can detect an external uniform force with much higher sensitivity with respect to bandgap modes of the soft-clamped membrane. This is due to the peculiarity of soft-clamped membranes, where the matching of the defect modes and the phonon modes produce a modal shape that is confined in the defect area, as it is shown in Fig. 5 for bandgap mode A. On the contrary, the axisymmetric modal shapes $(0, n)$ of round-shaped membranes are distributed over the whole membrane and allow a better matching of the modal shape with the uniform force field, even though their sensitivity decreases with the number of circumferential nodes. An estimation of S/N in the case of specific force signals goes beyond the scope of the article.

VII. CONCLUSIONS

Freestanding nano-membranes initially became widespread as windows for the chemical analysis by x ray, e-beam, and TEM, but recent studies have shown how useful they can be as a highly coherent mechanical resonator in the field of quantum technologies and fundamental physics. In these optomechanical systems, the membrane is embedded in a Fabry–Pérot optical cavity, where the radiation pressure couples the membrane's mechanical displacement with the intracavity field. The high value of the mechanical quality factor, at cryogenic and room temperatures, guarantees basic requirements for many challenging experiments, such as ground-state sideband cooling, quantum non-demolition measurements, and quantum squeezing of resonator states. Recent efforts are directed toward the functionalization of SiN membranes to allow coupling

with external signals. We mention, for instance, the deposition of a metal layer for the realization of device capable of converting RF/microwaves to optical signals, possibly at the quantum limit.[6]

In this work, we investigated the mechanical dissipation of two state-of-the-art membrane-based devices used in quantum optomechanical experiments, both produced in our microfabrication facility. They are based on tensioned SiN membranes, with equal thickness and stress, and reach high Q-factors thanks to the dissipation dilution effect.[15] Concepts based on stress/strain engineering and soft-clamping were used in the design to preserve this feature from the influence of the environment. A general design framework is outlined and discussed, showing advantages and drawbacks. We described the fabrication processes based on bulk/surface silicon micromachining and discussed our experimental results in the context of literature data.

Resonators with soft-clamping ensure the achievements of very high Q factor for a number of modes inside the bandgap; on the other hand, we have observed that they are more fragile, as imperfections in the holes' edge can trigger the membrane failure during the release phase, handling, or dicing. Currently, in the outcomes of our production process, the soft-clamped membranes are more sensitive to fabrication issues and we are reviewing the process to increase reproducibility and yield.

Round-shaped membrane with loss shield constitutes a reliable platform for optomechanical experiments, with modal Q-factor almost constant over a large frequency band, but did not demonstrate quality factor higher than 10^7. In this case, we are studying how to apply a stress engineering approach to increase the quality factor for a membrane while maintaining a membrane thickness of 100 nm in the central region, as it is needed to facilitate coupling with the laser beam.

We have completed our comparison with the evaluation of the interaction with an external force. As usual, we define the force sensitivity as the ratio between the thermal noise PSD and the square of the response function to the force. In the calculation, we neglect back-action noise from the readout. The analysis show that the sensitivity is strongly dependent on the design of a device, with soft-clamped membranes better suited for the detection of point forces while round-shaped membranes have the best performance in the detection of uniform force fields. This issue is relevant in proposals aiming to use low-loss resonators in the detection of dark matter signatures,[36] with an approach similar to that developed for a massive antenna.[37] We also note that in round-shaped membranes, the Q-factor is obtained for a large number of modes, providing an ideal platform for multimode quantum optomechanics or multimode sensing.[6]

ACKNOWLEDGMENTS

Research was performed within the Project QuaSeRT funded by the QuantERA ERA-NET Cofund in Quantum Technologies implemented within the European Union's Horizon 2020 Programme. The research has been partially supported by INFN (HUMOR project).

APPENDIX A: TENSILE AND BENDING STORED ENERGIES OF A ROUND-SHAPED MEMBRANE

We focus on axisymmetric modes for the sake of simplicity. The procedure is an extension to round-shaped membranes of the approach in Ref. 17 and developed for the doubly clamped nanostrings. The approximating function of a vibrational mode with modal index (0,n) can be decoupled into two contributions:

(a) in region $0 \le r \le R - \delta R$, the solution is the Bessel function of a simply supported vibrating plate,

$$w_{0n}(r) = k_{0n} J_0\left(\alpha_{0n}\frac{r}{R}\right), \tag{A1}$$

(b) in region $R \le r \le R - \delta R$, the solution is the deflection of a circular plate under circumferential load[38] and with a clamped edge,

$$u_{0n}(r) = \frac{P_{0n}}{8\pi D_z}(R^2 - r^2)\left(\frac{R^2 + (R-\delta R)^2}{2R^2} + ((R-\delta R)^2 + r^2)\ln\left(\frac{r}{R}\right)\right), \tag{A2}$$

where $R - \delta R$ is the value along the radial coordinate where the two modal shape functions have the same derivative,

$$\left.\frac{\partial w_{0n}}{\partial r}\right|_{r=R-\delta R} = \left.\frac{\partial u_{0n}}{\partial r}\right|_{r=R-\delta R}. \tag{A3}$$

The circumferential force load P_{0n} is related to membrane stress according to the following relation (see Fig. 18):

$$\frac{Q_{0n}}{\sigma h} = -\left.\frac{\partial w_{0n}}{\partial r}\right|_{r=R-\delta R}, \tag{A4}$$

where $Q_{0n} = P_{0n}/(2\pi(R - \delta R))$ and

$$P_{0n} = 2\pi(R-\delta R)\sigma h \frac{k_{0n}\alpha_{0n}J_1(\alpha_{0n})}{R}, \tag{A5}$$

where J_1 is the Bessel first order. Using Eqs. (A1) and (A2) in Eq. (A3) and neglecting δR^2, the thickness of the annular region becomes

$$\delta R = \sqrt{\frac{2D}{\sigma h}}, \tag{A6}$$

where D is the circular-plate flexural rigidity $D = \frac{1}{12}\frac{Y}{1-\nu^2}h^3$. Equation (A6) is similar to the expression of the critical length of a 1D string described in Ref. 16. Energy terms can be calculated with

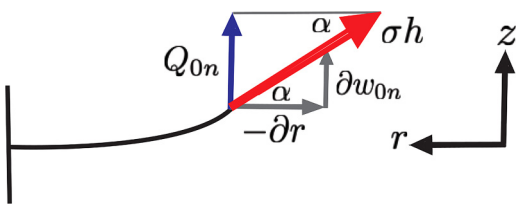

FIG. 18. Graphical representation of the membrane's tensile force decomposition.

the following formulas:

$$W_{tens} = \frac{1}{2}\sigma h \int_0^{2\pi} d\theta \int_0^R \left(\frac{\partial w_{0n}}{\partial r}\right)^2 r dr = \pi\sigma h \int_0^R \left(\frac{\partial w(r,n)}{\partial r}\right)^2 r dr, \quad \text{(A7)}$$

where W_{tens} is elastic energy stored in membrane tension. The stored bending energy due to the mean curvature of the membrane can be decoupled into following two contributions:

$$W_{bend-internal} = \frac{D}{2}\int_0^{2\pi} d\theta \int_0^R \left(\frac{\partial^2 w_{0n}}{\partial r^2} + \frac{1}{r}\frac{\partial w_{0n}}{\partial r}\right)^2 r dr = \pi D \int_0^R \left(\frac{\partial^2 w_{0n}}{\partial r^2} + \frac{1}{r}\frac{\partial w_{0n}}{\partial r}\right)^2 r dr, \quad \text{(A8)}$$

$$W_{bend-edge} = \frac{D}{2}\int_0^{2\pi} d\theta \int_{R-\delta R}^R \left(\frac{\partial^2 u_{0n}}{\partial r^2} + \frac{1}{r}\frac{\partial u_{0n}}{\partial r}\right)^2 r dr = \pi D \int_{R-\delta R}^R \left(\frac{\partial^2 u_{0n}}{\partial r^2} + \frac{1}{r}\frac{\partial u_{0n}}{\partial r}\right)^2 r dr. \quad \text{(A9)}$$

APPENDIX B: BENDING RADIAL STRAIN IN ROUND-SHAPED MEMBRANES

According to the von Karman theory of plates and considering the axisymmetric case, the radial flexural strain in polar coordinates can be written as

$$\varepsilon_{rr} = -z\frac{\partial^2 w_{0n}}{\partial r^2} \quad \text{(B1)}$$

in the region $0 \le r \le R - \delta R$, while

$$\varepsilon^*_{rr} = -z\frac{\partial^2 u_{0n}}{\partial r^2} \quad \text{(B2)}$$

in $R - \delta R \le r \le R$.

APPENDIX C: FITTING MODEL OF $Q \times \nu$ DATA FOR ROUND-SHAPED MEMBRANES

The Q-factor of a round-shaped membrane can be approximated by Eq. (5) considering an equivalent square-shaped membrane with the side equal to the diameter $L = D = 2R$. Using $m^2 + n^2 = 4\rho\nu^2 D^2$, the fitting model becomes

$$Q \times \nu = \frac{\nu\, Q_{int}}{\frac{\pi^2\nu^2 h^2 \rho Y}{3\sigma_0^2} + \frac{h\sqrt{\frac{Y}{\sigma_0}}}{\sqrt{32R}}}. \quad \text{(C1)}$$

For the SiN membrane, assume $Y = 270$ GPa, $\rho = 2800$ Kg/m^3, D=1680 μm, h = 100 nm, and $\sigma_0 = 0.918$ GPa. The fitting curve is derived using the least-square approach with free parameter Q_{int},

$$Q \times \nu = \frac{0.005\,842\,9\ \nu}{0.000\,589\,374 + 2.951\,31 \times 10^{-17}\nu^2}\ \text{(THz)} \quad \text{(C2)}$$

and ν expressed in (MHz). The best-fitting parameter value is $Q_{int} = 5842.9$, which is consistent with those found in Ref. 27 for Si_3N_4 membranes.

DATA AVAILABILITY

The data that support the findings of this study are available from the corresponding author upon reasonable request.

REFERENCES

[1]M. Rossi, D. Mason, J. Chen, Y. Tsaturyan, and A. Schliesser, Nature **563**, 53–58 (2018).
[2]D. Mason, J. Chen, M. Rossi, Y. Tsaturyan, and A. Schliesser, Nat. Phys. **15**, 745 (2019).
[3]A. Pontin, M. Bonaldi, A. Borrielli, L. Marconi, F. Marino, G. Pandraud, G. A. Prodi, P. M. Sarro, E. Serra, and F. Marin, Phys. Rev. A **97**, 033833 (2018).
[4]M. Bawaj, C. Biancofiore, M. Bonaldi, F. Bonfigli, A. Borrielli, G. Di Giuseppe, L. Marconi, F. Marino, R. Natali, A. Pontin, G. A. Prodi, E. Serra, D. Vitali, and F. Marin, Nat. Commun. **6**, 7503 (2015).
[5]A. Pontin, M. Bonaldi, A. Borrielli, F. S. Cataliotti, F. Marino, G. A. Prodi, E. Serra, and F. Marin, Phys. Rev. A **89**, 023848 (2014).
[6]I. Moaddel Haghighi, N. Malossi, R. Natali, G. Di Giuseppe, and D. Vitali, Phys. Rev. Appl. **9**, 034031 (2018).
[7]R. W. Andrews, R. W. Peterson, T. P. Purdy, K. Cicak, R. W. Simmonds, C. A. Regal, and K. W. Lehnert, Nat. Phys. **10**, 321 (2014).
[8]M. Aspelmeyer, T. J. Kippenberg, and F. Marquardt, Rev. Mod. Phys. **86**, 1391 (2014).
[9]F. Tebbenjohanns, M. Frimmer, V. Jain, D. Windey, and L. Novotny, Phys. Rev. Lett. **123**, 013603 (2020).
[10]U. Delić, M. Reisenbauer, K. Dare, D. Grass, V. Vuletić, N. Kiesel, and M. Aspelmeyer, Science **367**, 892 (2020).
[11]L. Magrini, P. Rosenzweig, C. Bach, A. Deutschmann-Olek, S. G. Hofer, S. Hong, N. Kiesel, A. Kugi, and M. Aspelmeyer, arXiv:2012.15188.
[12]A. Ranfagni, P. Vezio, M. Calamai, A. Chowdhury, F. Marino, and F. Marin, arXiv:2012.15265.
[13]A. Pontin, M. Bonaldi, A. Borrielli, F. S. Cataliotti, F. Marino, G. A. Prodi, E. Serra, and F. Marin, Phys. Rev. Lett. **112**, 023601 (2014).
[14]A. Chowdhury, P. Vezio, M. Bonaldi, A. Borrielli, F. Marino, B. Morana, G. A. Prodi, P. M. Sarro, E. Serra, and F. Marin, Phys. Rev. Lett. **124**, 023601 (2020).
[15]P. R. Saulson, Phys. Rev. D **42**, 2437 (1990).
[16]Q. P. Unterreithmeier, T. Faust, and J. P. Kotthaus, Phys. Rev. Lett. **105**, 027205 (2010).
[17]S. Schmid, K. D. Jensen, K. H. Nielsen, and A. Boisen, Phys. Rev. B **84**, 165307 (2011).
[18]M. Bückle, V. C. Hauber, G. D. Cole, C. Gartner, U. Zeimer, J. Grenzer, and E. M. Weig, Appl. Phys. Lett. **113**, 201903 (2018).
[19]S. Ghaffari, S. A. Chandorkar, S. Wang, E. J. Ng, C. H. Ahn, V. Hong, Y. Yang, and T. W. Kenny, Sci. Rep. **3**, 3244 (2013).
[20]A. Borrielli, L. Marconi, F. Marin, F. Marino, B. Morana, G. Pandraud, A. Pontin, G. A. Prodi, P. M. Sarro, E. Serra, and M. Bonaldi, Phys. Rev. B **94**, 121403 (2016).
[21]Y. Tsaturyan, A. Barg, E. S. Polzik, and A. Schliesser, Nat. Nanotechnol. **12**, 776 (2017).
[22]D. R. Southworth, R. A. Barton, S. S. Verbridge, B. Ilic, A. D. Fefferman, H. G. Craighead, and J. M. Parpia, Phys. Rev. Lett. **102**, 225503 (2009).
[23]P. L. Yu, T. P. Purdy, and C. A. Regal, Phys. Rev. Lett. **108**, 083603 (2012).
[24]L. Meirovitch, *Methods of Analytical Dynamics* (McGraw-Hill, New York, 1970).
[25]S. A. Fedorov, N. J. Engelsen, A. H. Ghadimi, M. J. Bereyhi, R. Schilling, D. J. Wilson, and T. J. Kippenberg, Phys. Rev. B **99**, 054107 (2019).

[26]M. J. Bereyhi, A. Beccari, S. A. Fedorov, A. H. Ghadimi, R. Schilling, D. J. Wilson, N. J. Engelsen, and T. J. Kippenberg, Nano Lett. **19**, 2329 (2019).
[27]L. G. Villanueva and S. Schmid, Phys. Rev. Lett. **113**, 227201 (2014).
[28]E. Serra, B. Morana, A. Borrielli, F. Marin, G. Pandraud, A. Pontin, G. A. Prodi, P. M. Sarro, and M. Bonaldi, IEEE J. Microelectromech. Syst. **27**, 1193 (2018).
[29]G. Gopalakrishnan, D. A. Czaplewski, K. M. McElhinny, M. V. Holt, J. C. Silva-Martínez, and P. G. Evans, Appl. Phys. Lett. **102**, 033113 (2013).
[30]E. Serra, M. Bawaj, A. Borrielli, G. Di Giuseppe, S. Forte, N. Kralj, N. Malossi, L. Marconi, F. Marin, F. Marino, B. Morana, R. Natali, G. Pandraud, A. Pontin, G. A. Prodi, M. Rossi, P. M. Sarro, D. Vitali, and M. Bonaldi, AIP Adv. **6**(6), 065004 (2016).
[31]A. Chowdhury, P. Vezio, M. Bonaldi, A. Borrielli, F. Marino, B. Morana, G. Pandraud, A. Pontin, G. A. Prodi, P. M. Sarro, E. Serra, and F. Marin, Quantum Sci. Technol. **4**, 024007 (2019).
[32]P. Vezio, A. Chowdhury, M. Bonaldi, A. Borrielli, F. Marino, B. Morana, G. A. Prodi, P. M. Sarro, E. Serra, and F. Marin, Phys. Rev. A **102**, 053505 (2020).
[33]M. Bonaldi, A. Borrielli, A. Chowdhury, G. Di Giuseppe, W. Li, N. Malossi, F. Marino, B. Morana, R. Natali, P. Piergentili, G. A. Prodi, P. M. Sarro, E. Serra, P. Vezio, D. Vitali, and F. Marin, Eur. Phys. J. D **74**, 178 (2020).
[34]M. Bonaldi, M. Cerdonio, L. Conti, P. Falferi, P. Leaci, S. Odorizzi, G. A. Prodi, M. Saraceni, E. Serra, and J. P. Zendri, Phys. Rev. D **7**, 022003 (2006).
[35]Y. Levin, Phys. Rev. D **57**, 659 (1998).
[36]D. Carney, G. Krnjaic, D. C. Moore, and C. A. Regal, Quantum Sci. Technol. **6**, 024002 (2021).
[37]A. Branca, M. Bonaldi, M. Cerdonio, L. Conti, P. Falferi, F. Marin, R. Mezzena, A. Ortolan, G. A. Prodi, L. Taffarello *et al.*, Phys. Rev. Lett. **118**, 021302 (2017).
[38]S. Timoshenko and S. Woinowsky-Krieger, *Theory of Plates and Shells* (McGraw-Hill, New York, 1959).